Shallow-water models with anisotropic porosity and merging for flood modelling on Cartesian grids

M. Bruwier[a], P. Archambeau, S. Erpicum, M. Pirotton & B. Dewals

Hydraulics in Environmental and Civil Engineering (HECE), University of Liege (ULG), Belgium

Allée de la Découverte 9 (B52/3) 4000 Liege, Belgium

[a] *Corresponding author: mbruwier@ulg.ac.be, +3243669004*

ABSTRACT:

Shallow-water models with porosity are used to compute floods at a relatively coarse resolution while accounting indirectly for detailed topographic data through porosity parameters. In many practical applications, these models enable a significant reduction of the computational time while maintaining an acceptable level of accuracy. In this paper, we improve the use of porosity models on Cartesian grids by three original contributions. First, a merging technique is used to handle cells with low porosity values which tend otherwise to seriously hamper computational efficiency. Next, we show that the optimal method for the determination of the porosity parameters depends on the modelling scale, i.e. the grid resolution compared to the characteristic size of obstacles and flow ways. Finally, we investigate the potential benefit of using a different porosity parameter in each term of the shallow-water equations. Five test cases, two of them being original, are used to validate the model and assess each contribution. In particular, we obtained speedup values between 10 and 100 while the errors on water depths remain around few percent.

Keywords: Porosity model, Cartesian grid, Merging, Urban floods modelling.

1 INTRODUCTION

With an estimated cumulated damage of 100 billion euros in Europe over the period 1986 - 2006 and over 1,100 casualties between 1998 and 2009, floods remain the most common natural hazard

(De Moel et al., 2009; EEA, 2010). Adequate flood risk management must be based on reliable estimates of both flood hazard and flood vulnerability. A key component of the former is the computation of flow characteristics in the floodplains as they have a direct influence on flood impacts (Brazdova and Riha, 2014; Kreibich et al., 2014; Kellermann et al., 2015).

Shallow-water models are recognized as state-of-the-art for conducting inundation modelling for large scale real-world applications (El Kadi Abderrezzak et al., 2009; Costabile and Macchione, 2015). The flow characteristics computed by such models are strongly affected by the quality of topographic data and by the relative size of the numerical model resolution compared to the typical size of obstacles and flow ways in the floodplains (Dottori et al., 2013). Today, topographic data have become widely available at a scale as fine as a few metres. While such high-resolution topographic data enable in principle the computation of surface flow variables with a high accuracy, solving the shallow-water equations at the metre-scale may become hardly tractable due to the computational burden.

In the following, we distinguish between three different modelling scales, as sketched in Figure 1 in the case of a Cartesian grid:

- *micro-scale*, i.e. all obstacles are resolved explicitly and with a fairly good accuracy (e.g., with about ten cells over the typical width of flow paths);
- *meso-scale*, i.e. the obstacles are explicitly represented by “holes” in the computational domain (as described by Schubert and Sanders, 2012); but they are poorly resolved (e.g., with just a couple of cells over the typical width of flow paths);
- *macro-scale*, i.e. the obstacles have a typical size comparable or smaller than the mesh size (e.g., the flow paths are generally smaller than the size of one computational cell).

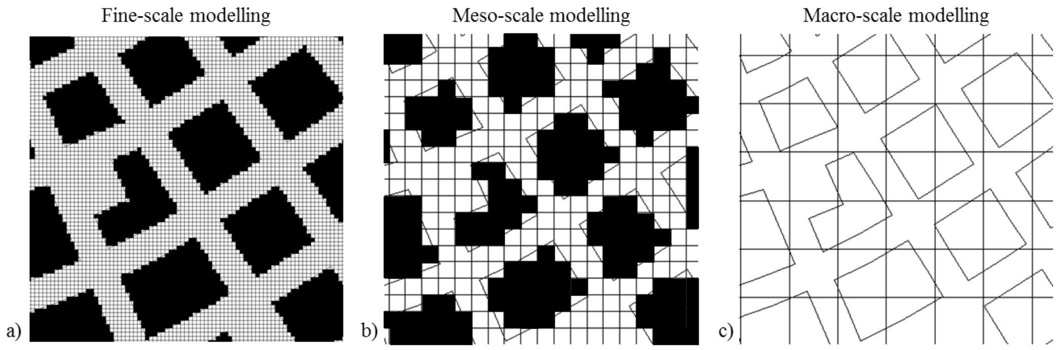

Figure 1: Definition of (a) fine-scale, (b) meso-scale and (c) macro-scale modelling and representation of the obstacles explicitly represented by holes in the computational domain (dark cells).

Depending on the study objectives, meso-scale and/or macro-scale modelling may prove useful for inundation modelling over particularly large areas, or when a high number of model runs is necessary (scenario analysis, stochastic modelling …). In such cases, *subgrid models* may be used to enhance the results accuracy. Subgrid models enable grid coarsening, while preserving to some extent the detailed topographic information.

Porosity models are one kind of subgrid models, in which fine-scale topographic information is reproduced at a coarser scale through porosity parameters. The role of these porosity parameters is to mimic at the coarse scale the influence of the unresolved subgrid obstacle features on the different terms of the shallow-water equations.

Some authors use the same porosity to reproduce the effect of obstacles on the conserved variables and on the flux terms of the shallow-water equations (Guinot and Soares-Frazão, 2006). Such *isotropic porosity models* are based on a single porosity parameter ϕ_{REV} at the scale of a *Representative Elementary Volume* (REV), as detailed by Sanders et al. (2008). However, the scale required to obtain a REV is generally much greater than the cell size (Guinot, 2012) which makes the determination of the isotropic porosity challenging.

Sanders et al. (2008) developed an *anisotropic integral porosity model* (IP) in which two types of porosity parameters are distinguished: a storage porosity ϕ (cell property) reflects the cell storage capacity and a conveyance porosity ψ (edge property) reflects the effect of obstacles on the flux terms. The storage porosity is evaluated as the geometrical void fraction within a cell. The conveyance porosity is computed as the void fraction along an edge, leading to conveyance porosities very sensitive to the mesh design. For this reason, Sanders et al. (2008) recommend the use of a *gap-conforming mesh* in which the mesh intersects optimally the obstacles to capture the conveyance effects of these obstacles. Since the porosity parameters are explicitly mesh-dependent, the governing equations are written directly in a discretized form. Recently, Guinot et al. (2017) proposed a *dual integral porosity model* (DIP), which outperforms the anisotropic integral porosity model. It distinguishes cell-based and edge-based flow variables, and it involves a transient momentum dissipation model.

The use of Cartesian grids is of practical relevance (Kim et al., 2014) as it makes the computational mesh consistent with commonly available gridded data, as obtained from most remote sensing techniques. Moreover, explicit numerical schemes computed on Cartesian grids are well adapted for parallelization techniques like GPUs (Brodtkorb et al., 2012). In this paper, similarly to the integral porosity models, we start directly from the discretized form of the equations and we make three new contributions to improve the application of the porosity models on Cartesian grids.

- For stability reasons, the computational time may dramatically increase in the presence of cells with a very low storage porosity. As a first contribution, this paper introduces a *merging technique* to address this issue.
- Up to now, anisotropic porosity models were preferably used with unstructured meshes as they require a gap-conforming mesh for the determination of the conveyance porosity (Kim et al., 2014). As a second contribution, we compare the standard method determining the conveyance porosity directly along edges of the computational cells (footprint method) to an original approach taking into account the presence of obstacles in a region defined around the edge. We show that the performance of the two methods are influenced by the relative sizes of the computational cells compared to the obstacles (meso- vs. macro-scale modelling).

- In general terms, porosity parameters should be different in each term of the governing equations to reproduce optimally the effects of obstacles at a coarse scale. As a third contribution, the potential benefit of distinguishing the porosity parameters in the various terms of the governing equations is explored here for an idealized urban network.

The governing equations of the models with anisotropic porosity are introduced in sections 2.1 (integral form) and 2.2 (discrete form). The numerical resolution of the governing equations is presented in section 3. The new contributions are evaluated based on test cases in section 4.

2 GOVERNING EQUATIONS

2.1 *Integral form*

The integral form of the porous two-dimensional shallow-water equations writes for a control volume as (Sanders et al., 2008; Guinot et al., 2017):

$$\frac{\partial}{\partial t}\int_{\Omega} i\,\mathbf{U}\,d\Omega + \int_{\partial\Omega} i\,\mathbf{M}\,\mathbf{F}\cdot\mathbf{n}\,d\partial\Omega = \int_{\Omega} i\,\mathbf{S}\,d\Omega \tag{1}$$

with Ω the total horizontal surface of the control volume, $\partial\Omega$ the boundary of the control volume, t the time, $\mathbf{n} = \left[n_x, n_y\right]^T$ the x- and y-normal unit vector components and i the binary phase function equal to 0 where obstacles stand and to 1 in the voids.

The conserved vector variable $\mathbf{U}$, the momentum dissipation term $\mathbf{M}$, the fluxes $\mathbf{F}$ and the source term $\mathbf{S}$ are:

$$\mathbf{U} = \begin{bmatrix} h \\ uh \\ vh \end{bmatrix}, \qquad \mathbf{M} = \begin{bmatrix} 1 & 0 & 0 \\ 0 & 1-\mu_{xx} & -\mu_{xy} \\ 0 & -\mu_{yx} & 1-\mu_{yy} \end{bmatrix},$$
$$\mathbf{F} = \begin{bmatrix} uh & vh \\ u^2 h + \frac{1}{2} g\left(h^2 - h_{\eta_{0,x}}^2\right) & uvh \\ uvh & v^2 h + \frac{1}{2} g\left(h^2 - h_{\eta_{0,y}}^2\right) \end{bmatrix}, \qquad \mathbf{S} = -\begin{bmatrix} 0 \\ \left(c_D^f + c_{D,xx}^b + c_{D,xy}^b\right) uV \\ \left(c_D^f + c_{D,yy}^b + c_{D,yx}^b\right) vV \end{bmatrix}, \tag{2}$$

with h the water depth, u and v the x- and y-velocity components, $V = \sqrt{u^2 + v^2}$, g the gravitational acceleration, μ_{xx} , μ_{xy} , μ_{yx} and μ_{yy} the components of the transient momentum dissipation tensor, c_D^f the roughness coefficient, $c_{D,xx}^b$, $c_{D,xy}^b$, $c_{D,yx}^b$ and $c_{D,yy}^b$ the components of the drag tensor accounting for the resistance of obstacles to the flow. The term $gh_{\eta_0}^2/2$ corresponds to the divergence formulation of the bed slope term with h_{η_0} representing a water depth evaluated for a piecewise stationary water level $\eta = \eta_0$, as detailed in section 3.1 (Valiani and Begnudelli, 2006).

The transient momentum dissipation tensor was introduced by Guinot et al. (2017). It improves the reproduction of the propagation speed of a positive wave, at the expense of an additional parameter to be calibrated. Here, we focus mostly on steady and quasi-steady flow configurations, so that this tensor does not need to be considered ($\mu_{xx} = \mu_{xy} = \mu_{yx} = \mu_{yy} = 0$); except in our fifth test case focusing on wave propagation (section 4.5).

The drag tensor formulation introduced in Eq. (2) reflects the anisotropic nature of the drag force. However, in the following, we opt for a simplified scalar formulation (i.e. assuming $c_{D,xy}^b = c_{D,yx}^b = 0$ $c_{D,xx}^b = c_{D,yy}^b$), as originally used by Sanders et al. (2008):

$$c_{D,xx}^b = c_{D,yy}^b = \frac{c_D^0 a h}{2} \ , \tag{3}$$

where c_D^0 is a dimensionless drag coefficient and a denotes the width of obstructions in the direction normal to the flow, per unit of planform area. This scalar drag formulation is a substantial limitation of the present study, as further discussed in section 4.2.4. Recently, a more advanced head loss model was proposed by Velickovic et al. (2017). The model was tested for networks of perpendicular streets constituted by arrays of 5 × 5 aligned buildings. Based on a generalized tensor formulation and a so-called amplification factor, it accounts explicitly for the non-alignment of the main streets to the main flow direction and for the deviation of the bulk velocity to the direction of the streets. Nonetheless, further work is required to adapt the methodology and the calibration strategy to more general configurations.

2.2 *Discrete form*

Over a computational cell *j*, the average water depth $\langle h \rangle_j$ and unit discharges $\langle uh \rangle_j$ and $\langle vh \rangle_j$ are defined as:

$$\langle h \rangle_j = \frac{\int_{\Omega_j} ih \, d\Omega}{\int_{\Omega_j} i \, d\Omega}; \quad \langle uh \rangle_j = \frac{\int_{\Omega_j} iuh \, d\Omega}{\int_{\Omega_j} i \, d\Omega}; \quad \langle vh \rangle_j = \frac{\int_{\Omega_j} ivh \, d\Omega}{\int_{\Omega_j} i \, d\Omega} \tag{4}$$

Based on Eq. (4), other average variables can be deduced:

$$\langle u \rangle_j = \frac{\langle uh \rangle_j}{\langle h \rangle_j}; \quad \langle v \rangle_j = \frac{\langle vh \rangle_j}{\langle h \rangle_j}; \quad \langle V \rangle_j = \sqrt{\langle u \rangle_j^2 + \langle v \rangle_j^2} \tag{5}$$

Porosity parameters of the cell are defined as:

$$\phi_j = \frac{1}{\Omega_j} \int_{\Omega_j} i \, d\Omega; \quad \phi_{s_x,j} = \frac{\int_{\Omega_j} iuV \, d\Omega}{\langle uV \rangle_j \Omega_j}; \quad \phi_{s_y,j} = \frac{\int_{\Omega_j} ivV \, d\Omega}{\langle vV \rangle_j \Omega_j} \tag{6}$$

We introduce different edge porosity parameters for each type of flux term: ψ_c, ψ_{m,A_1}, ψ_{m,A_2} and $\psi_{m,P}$ respectively for the continuity flux term, the two advective terms and the pressure term. For a cell edge *k*, of length $\partial\Omega_k$, the edge porosity parameters are defined as:

$$\psi_{c,k} = \frac{\int_{\partial\Omega_k} iuh \, d\partial\Omega}{[uh]_k}; \; \psi_{mA_1,k} = \frac{\int_{\partial\Omega_k} iu^2h \, d\partial\Omega}{[u^2h]_k}; \; \psi_{mA_2,k} = \frac{\int_{\partial\Omega_k} iuvh \, d\partial\Omega}{[uvh]_k}; \; \psi_{mP,k} = \frac{\int_{\partial\Omega_k} h^2 \, d\partial\Omega}{[h^2]_k}, \tag{7}$$

where notation $[\ ]_k$ denotes the flow variables at the edges, as estimated by a piecewise constant reconstruction of the average values $\langle\ \rangle_j$ at the cells. The porosity parameters for the *y*- direction are defined similarly as for the *x*- direction.

Unlike standard definitions of the porosity, the parameters defined in Eq. (7) lump geometric effects, flow-related effects (similar to those reflected by Boussinesq coefficients in the usual shallow-water equations) and effects of the flow field reconstruction. Parameters $\phi_{s_x,j}$ and $\phi_{s_y,j}$, as defined in Eq. (6), also combine geometric and flow-related effects. Therefore, in the following, the quantities $\psi_{c,k}$, $\psi_{mA_1,k}$, $\psi_{mA_2,k}$, $\psi_{mP,k}$, $\phi_{s_x,j}$ and $\phi_{s_y,j}$ are all referred to as "porosity parameters" (instead of just "porosities").

Substituting definitions (4), (6) and (7) in Eq. (1) and considering the roughness and drag coefficients as uniform over each cell, the discrete formulation of the shallow water model with anisotropic porosity parameters writes as:

$$\frac{\partial \langle \mathbf{U} \rangle_j}{\partial t} + \frac{1}{\Omega_j} \sum_{k=1}^{K} [\mathbf{F}]_k \, \partial\Omega_k = \langle \mathbf{S} \rangle_j \tag{8}$$

where the discrete average variable $\langle \mathbf{U} \rangle$, average fluxes $[\mathbf{F}]$ and average source term $\langle \mathbf{S} \rangle$ are given by:

$$\begin{aligned}
&\langle \mathbf{U} \rangle = \phi \begin{bmatrix} \langle h \rangle \\ \langle uh \rangle \\ \langle vh \rangle \end{bmatrix}, \\
&[\mathbf{F}] = \begin{bmatrix} \psi_{c,x}[uh] & \psi_{c,y}[vh] \\ \psi_{mA_1,x}\left[u^2 h\right] + \psi_{mP,x}\dfrac{g}{2}\left([h]^2 - h_{\eta_0,x}^2\right) & \psi_{mA_2,y}[uvh] \\ \psi_{mA_2,x}[uvh] & \psi_{mA_1,y}\left[v^2 h\right] + \psi_{mP,y}\dfrac{g}{2}\left([h]^2 - h_{\eta_0,y}^2\right) \end{bmatrix}, \\
&\langle \mathbf{S} \rangle = -\begin{bmatrix} 0 \\ \phi_{s_x}\left(c_D^f + c_{D,x}^b\right)\langle uV \rangle \\ \phi_{s_y}\left(c_D^f + c_{D,y}^b\right)\langle vV \rangle \end{bmatrix}
\end{aligned} \tag{9}$$

Appendix A details the eigenvalue analysis of the system of governing equations for a one-directional flow over a horizontal and frictionless bottom. It shows that hyperbolicity of the system is ensured when $\psi_{mA_1} \geq \psi_c$.

In practice, the determination of each independent porosity parameter is challenging and may require an a priori knowledge of the flow field. For this reason, unless otherwise stated, the cell porosity ϕ_s is replaced in the following by the storage porosity ϕ while the edge porosity parameters ψ_c, ψ_{mA_1}, ψ_{mA_2} and ψ_{mP} are merged into a single conveyance porosity ψ. Under this assumption, Eqs (8) and (9) become identical to those derived by Sanders et al. (2008). Only in section 4.4, the potential improvement brought by discriminating the different edge porosity parameters is analysed for an idealized urban network. It is also discussed in section 4.5.

For the determination of the drag term, we use in the following the simplified formulation introduced by Schubert and Sanders (2012) to approximate parameter a independently from the flow direction:

$$a = \frac{1}{K\Omega}\sum_{k=1}^{K}\left(1-\psi_k\right)\partial\Omega_k \ , \tag{10}$$

where K is the number of edges.

3 NUMERICAL MODEL

3.1 *Spatial discretization*

The governing equations are solved with the hydraulic model Wolf2D using a first-order conservative finite volume scheme based on a flux vector splitting technique applied on a Cartesian grid (Erpicum et al., 2010). The piecewise stationary free surface elevations $\eta_{0,x}$ and $\eta_{0,y}$ used in the divergence formulation of the bed slope term are evaluated as a linear combination of the free surface levels at the edges of the computational cell. The weighting factors in the linear combination are chosen to minimize the error in the energy balance, as detailed by Bruwier et al. (2016).

3.2 *Time discretization*

The time integration is performed using an explicit Runge-Kutta method. The stability of the scheme is ensured by a Courant-Friedrichs-Lewy criterion, modified by Sanders et al. (2008) to consider the porosity parameters. The criterion writes:

$$\Delta t \le CFL \min_j \left(\frac{\phi_j \Omega_j}{\max_K (\psi_k \partial\Omega_k)} \frac{1}{c_j} \right), \tag{11}$$

where Δt is the time step, $c_j = \sqrt{gh_j} + V_j$ the wave celerity of cell j, CFL the Courant number depending on the Runge-Kutta method.

3.3 *Models summary*

Depending on the method used for the determination of the porosity parameters, different porosity-based models can be derived from the governing equations (8) and (9), as detailed in Table 1.

If all porosity parameters are set to unity, the classical shallow-water model (CS model) is retrieved.

If the storage and edge porosity parameters are set to the same value ϕ_{REV}, the isotropic porosity model (PS-I) is obtained.

If different values are used for the storage and edge porosity parameters, the model becomes anisotropic (PS-A). Different PS-A models can be derived depending on how the edge porosity parameters are evaluated:

- The standard approach in literature is based on a direct determination of a single conveyance porosity as the linear void fraction along each computational edge, which make it highly mesh-dependent. Here, this approach is referred to as model PS-A-1.
- While the gap-conforming property required for PS-A-1 models can be ensured using an unstructured mesh (Sanders et al., 2008), this is hardly feasible based on a Cartesian grid, as used here. Indeed, the determination of the conveyance porosities directly along the edges can fail to detect the presence of nearby obstacles, as highlighted by Chen et al. (2012) and

Özgen et al. (2016). For this reason, we compare the PS-A-1 model to an original method, which consists in relating the conveyance porosity of an edge to the minimum fraction of free length parallel to this edge over half a computational cell on either sides of the edge (Figure 2). We call this model PS-A-2. Although this model remains mesh-dependent to some extent, the porosity parameters are less sensitive to the mesh design than those of the PS-A-1 model.

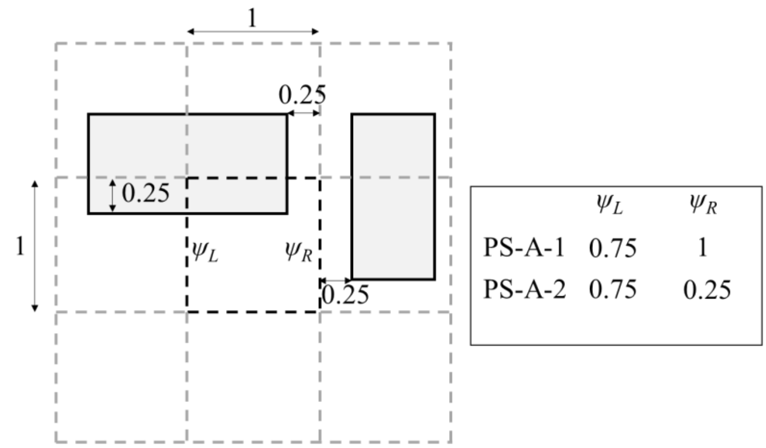

Figure 2: Example of determination of conveyance porosities with the PS-A-1 and PS-A-2 models.

In the case of meso-scale modelling (Figure 1b), the mesh is close to be gap-conforming and the PS-A-1 model is therefore expected to perform well (Arrault et al., 2016). In contrast, in the case of macro-scale modelling (Figure 1c), the obstacles are generally reproduced on the coarse grid only through the porosity parameters since they are not resolved explicitly. The mesh is mainly non gap-conforming and the PS-A-2 model is expected to improve the determination of the conveyance porosity parameters.

Finally, two models distinguish different edge porosity parameters ψ_c, ψ_{mA_1}, ψ_{mA_2} and ψ_{mP}:

- In the recent dual integral porosity model (DIP) of Guinot et al. (2017), the edge porosity parameters are obtained from a closure model based on mass conservation considerations and on the assumption that obstacles have a significant influence on flow velocity but a negligible one on the free surface elevation. The resulting edge porosity parameters are combinations of the storage and conveyance porosities, ϕ and ψ, as detailed in Table 1. In the following, this model is referred to as model PS-A-1-D.

- In one of the test cases (idealized urban network), we also introduce a model (PS-A-D model) in which the edge porosity parameters are estimated from an a priori estimation of the main flow characteristics, as detailed in section 4.4.

<table>
<tr><th>Acronym</th><th>Guinot et al. (2017)</th><th>Storage porosity</th><th>Edge porosity parameters</th><th>Evaluation of the edge porosity parameters</th></tr>
<tr><td>CS</td><td></td><td>1</td><td>1</td><td>/</td></tr>
<tr><td>PS-I</td><td>Single porosity model (SP)</td><td>ϕ_{REV}</td><td>ϕ_{REV}</td><td>/</td></tr>
<tr><td>PS-A-1</td><td>Integral porosity model (IP)</td><td rowspan="4">ϕ</td><td rowspan="2">ψ</td><td>Geometrically along the edge (footprint method)</td></tr>
<tr><td>PS-A-2</td><td></td><td>Minimum free length parallel to the edge over half a cell on either sides of the edge</td></tr>
<tr><td>PS-A-1-D</td><td>Dual integral porosity model (DIP)</td><td>$\psi_c = \phi$, $\psi_{m,A_1} = \frac{\phi^2}{\psi} = \psi_{m,A_2}$, $\psi_{m,P} = \psi$</td><td>Closure relation involving ϕ and ψ determined by the footprint method</td></tr>
<tr><td>PS-A-D</td><td></td><td>ψ_c, ψ_{m,A_1}, ψ_{m,A_2}, $\psi_{m,P}$</td><td>Based on an a priori estimation of the flow features</td></tr>
</table>

Table 1: Classification of the porosity models.

3.4 *Merging technique*

From the stability criterion given by Eq. (11), the time step is expected to decrease dramatically in the presence of very low values of the storage porosity. A crude approach to circumvent this problem consists in removing from the computational domain the cells having a storage porosity lower than a threshold $\phi_{\min}$. A more elaborate technique consists in *merging* such cells with neighbouring cells, following a similar approach as developed by Causon et al. (2000) for cutcells. This technique was adapted here. It follows a four-step procedure, as sketched in Figure 3:

1) Identify all computational cells with a storage porosity lower than a threshold $\phi_{\min}$ (cell C in Figure 3).
2) The low porosity cell is merged with the neighbouring cell sharing the border with the highest conveyance porosity (cell B). If several of these borders have the same conveyance porosity parameters, the merging is performed with the neighbouring cell having the lowest storage porosity. If several of these neighbouring cells have the same storage porosity, the merging is split evenly between all of them.
3) The merging of the cells consists in increasing the storage porosity of the neighbouring cell by the storage porosity of the low porosity cell. If the merging involves multiple neighbouring cells, the storage porosity of the low porosity cell is shared equally between the neighbouring cells.
4) The topology of the edges is also updated by the cell merging. In Figure 3, the right edge of cell D (DC) is connected to cell B while the left edge of cell B (AB) becomes connected to cells A and D (edge AB + DC). The bottom edge of cell B is set impervious.

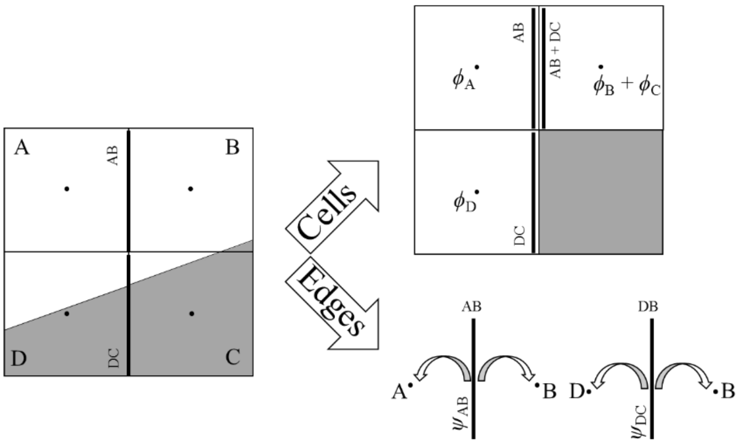

Figure 3: Representation of an application of the merging technique on cell C.

4 TEST CASES

Five test cases are presented in this section, two of them being original. As detailed in Table 2, each of the first four test cases enables assessing one specific contribution of the manuscript, while in the fifth test, the ability of the porosity model to reproduce wave propagation is assessed.

Based on a simple configuration involving a straight channel of varying orientation, the first original test case demonstrates the gain in efficiency and accuracy obtained thanks to the merging technique (section 4.1). This technique is then used in all subsequent test cases.

The second and third test cases (sections 4.2 and 4.3) aim at comparing different methods for the determination of the conveyance porosity parameters at meso- and macro- scale. In section 4.2, steady flows are computed in three synthetic but quasi-realistic urban networks. The PS-A-1 model is used for two urban networks discretized at the meso-scale. The PS-A-1 and PS-A-2 models are compared for the third urban network which lies at the transition between the meso-scale and the macro-scale. In section 4.3, the two models PS-A-1 and PS-A-2A are compared for the computation of a dam-break flow over an isotropic array of buildings discretized at the macro-scale.

Based on an idealized urban network, the fourth test case (section 4.4) shows the potential benefit of distinguishing the porosity parameters involved in each term of the governing equations (PS-A-D model). This test case also compares the PS-A-D model to the DIP model of Guinot et al. (2017).

In a fifth test case, the PS-A-D model is used with the transient momentum dissipation model introduced by Guinot et al. (2017) to reproduce a dam-break flow (positive and negative wave) over an idealized urban area.

Objective	Test case 1	Test case 2	Test case 3	Test case 4	Test case 5
Assess the merging technique	■	□	□	□	□
Compare different evaluations of the conveyance porosity for *meso-scale* modelling		■			
Compare different evaluations of the conveyance porosity for *macro-scale* modelling			■	■	
Explore the use of distinct porosity parameters in the various fluxes				■	□
Positive and negative wave propagation					■

Table 2: Overview of the five test cases and their specific objectives. Symbol ■ indicates that the corresponding model feature is tested systematically in the test case, while symbol □ refers to model features which are used in the test case but the test case is not specifically dedicated to their assessment.

In all test cases, the *average error* L is used as a metrics to quantify the difference between the results computed with the porosity models (w_1) and a set of N reference values (w_2):

$$L = \frac{1}{N}\sum_{i=1}^{N}\left|w_2 - w_1\right| \tag{12}$$

In line with Kim et al. (2015), we distinguish here five types of errors:

- the *structural model error* L_1 reflects the differences between micro-scale results and measurements;
- the *scale error* L_2 results from the averaging of the micro-scale results to the coarse scale (called hereafter “CS-P predictions”);
- combining errors L_1 and L_2, the *pore-scale error* L_{1+2} represents the differences between the CS-P predictions and measurements.
- the *coarse model error* L_3 corresponds to the difference between the results of a coarse scale model and the CS-P predictions. If the coarse scale model is a porosity model, error L_3 is called *porosity model error*;
- finally, the *total error* L_0 is obtained by comparing directly the (coarse) model results to the measurements.

Note that errors L_1, L_2 and L_{1+2} are independent of the considered porosity model.

4.1 *Rectangular channel with varying orientation*

4.1.1 *Description of the test case*

We first consider the simple configuration of a normal flow in a prismatic channel for a discharge Q. The channel is characterized by a rectangular cross-section of width W, a bed slope i, a length L and a Manning roughness coefficient n. The values of these parameters are taken as representative of one reach of a typical large river (Table 3).

Parameter	Symbol	Value
Length	L	15 km
Width	W	120 m
Longitudinal slope	i	0.2%
Manning roughness coefficient	n	0.025 sm$^{-1/3}$
Discharge	Q	2,000 m^3/s
Theoretical normal depth	h_u	2.517 m
Mesh size	Δx	30 m

Table 3: Parameters of the rectangular channel.

Using a shallow-water model on a Cartesian grid and prescribing the normal depth h_u as a downstream boundary condition, the computed water depths remain equal to h_u all along the channel if the channel is oriented along the Cartesian grid (Figure 4a). In contrast, if the channel is not aligned with the grid (Figure 4b), the computed water depths are higher than the theoretical normal depth and the flow variables fluctuate spatially due to abrupt changes of cross-section resulting from the banks discretization. At some distance from the downstream end of the channel, the computed depths along the centreline fluctuate around a mean value $\hat{h}_u$ (Figure 5), which we consider here as a “numerical” normal depth.

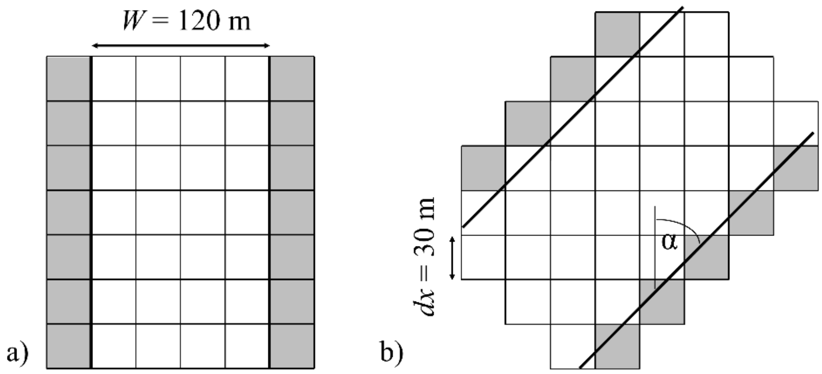

Figure 4: (a) Channel aligned with the grid (α = 0°) and (b) channel of a different orientation than the grid, leading to artificial changes of cross-section in the numerical discretization.

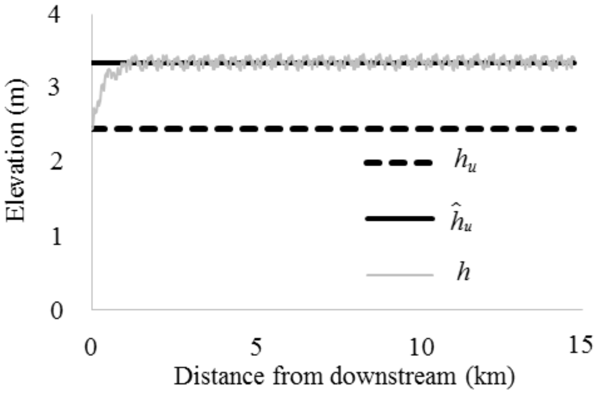

Figure 5: Spatial variation of the water depth h along the centreline of the channel, theoretical normal water depth h_u and numerical normal water depth $\hat{h}_u$ (angle α = 15°).

In the following, we compare the numerical normal depth $\hat{h}_u$ to the theoretical one h_u using the ratio $\hat{h}_u/h_u$.

4.1.2 *Classical shallow-water model vs. porosity-based model*

Simulations were performed for an orientation of the channel varying between α = 0° and α = 45°, with a step of 1°. Using the CS model, the numerical normal depth $\hat{h}_u$ steadily increases when α is varied between 0° and 20° (Figure 6). The numerical values of the normal depth exceed the theoretical one by almost 40% for angles α in-between 20° and 35°. This overestimation is gradually reduced as α increases from 35° up to 45°.

The results of CS model are compared to those obtained with the PS-A-1 model. For all orientation angles α, the PS-A-1 model leads to numerical normal depths $\hat{h}_u$ much closer to the theoretical ones. In addition, the remaining overestimation of the normal depth decreases significantly when the threshold porosity $\phi_{\min}$ is reduced. This demonstrates the ability of the PS-A-1 model to compensate almost completely for the staircase effect resulting from the discretisation of the oblique boundaries of the channel on a Cartesian grid.

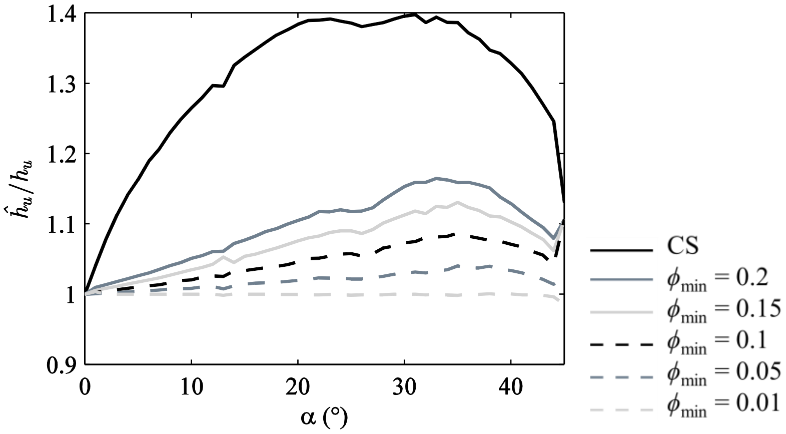

Figure 6: Numerical normal depth $\hat{h}_u$ compared to the theoretical one as a function of the orientation angle α, using the CS model and the PS-A-1 model for different threshold porosities ϕ_{min} (Δx = 30 m).

4.1.3 *Porosity model with merging*

When the merging technique is used, the computed normal depths $\hat{h}_u$ become much closer to the theoretical value h_u, even for relatively high values of ϕ_{min} (Figure 7 and Figure 8a). For instance, for a ϕ_{min} value of 0.2, the overestimation of h_u is reduced from ~16% (no merging) to ~1% (with merging). For low values of ϕ_{min}, the numerical normal depth is even underestimated with the PS-A-1 model with merging, but this underestimation does not exceed 5%.

For a given threshold porosity, the computational time (CT) with merging is slightly higher than without (Figure 8b). However, since the merging technique enables the use of much higher values of ϕ_{min} to reach a given accuracy, the benefit of this technique in terms of computation time is great. For instance, to limit the numerical error on h_u at 5%, a threshold porosity of ϕ_{min} = 0.05 is required without merging ($\max_{\alpha} |\hat{h}_u/h_u - 1| \approx 4\%$) while a value of ϕ_{min} = 0.75 may be used in combination with the merging technique ($\max_{\alpha} |\hat{h}_u/h_u - 1| \approx 3\%$) (Figure 8a). For these values, the PS-A-1 model without merging is 14.5 times computationally more expensive than the CS model, whereas the PS-A-1 model with merging is only 1.9 times more expensive.

Using a micro-scale CS model with cell sizes of 5 m (instead of 30 m), the maximum relative error $\max_{\alpha} |\hat{h}_u/h_u - 1|$ is around 11%. Since the computation cost scales theoretically with Δx^3, the computation time for the CS model with a cell size of 5 m is about 6^3 times higher than with the CS model with a cell size of 30 m, which is around two orders of magnitude slower than the PS-A-1 model with merging for a similar accuracy.

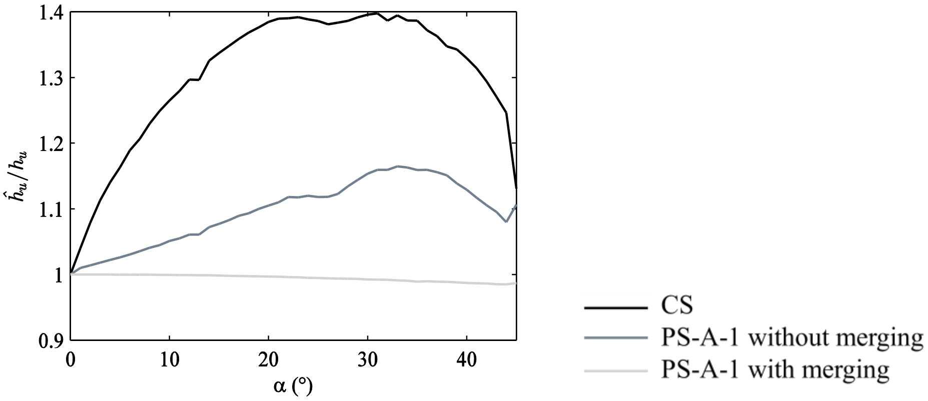

Figure 7: Numerical normal water depth $\hat{h}_u$ compared to the theoretical one as a function of the orientation angle α, using the CS model and PS-A-1 models without and with merging for $\phi_{\min} = 0.2$ ($\Delta x = 30$ m).

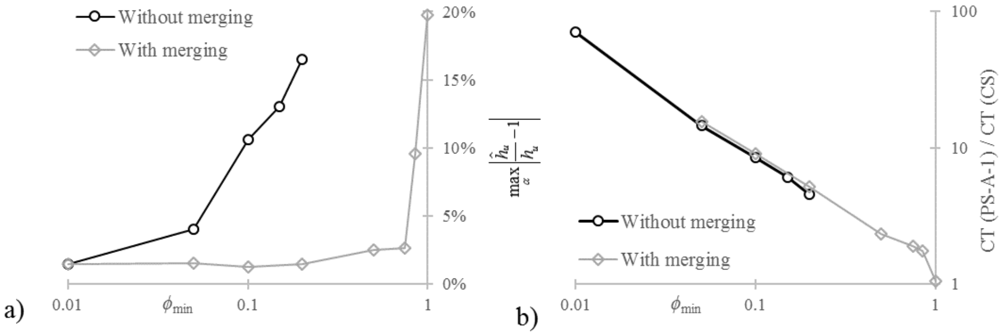

Figure 8: (a) Maximum relative error between the numerical normal depth $\hat{h}_u$ and the theoretical one h_u over all the orientation angles α for the PS-A-1 model without and with merging; (b) Ratio between the computational time (CT) of the PS-A-1 model without and with merging and the CT of the CS model as a function of the threshold porosity $\phi_{\min}$ ($\Delta x = 30$ m).

4.2 *Synthetic urban networks*

This original test case is based on three synthetic urban configurations (Figure 9) characterized by strongly contrasting geometric parameters (i.e. different streets widths and curvatures, buildings areas, building coverage ratios …). In Supplemental data, we provide data describing the geometry of the buildings in each urban configuration.

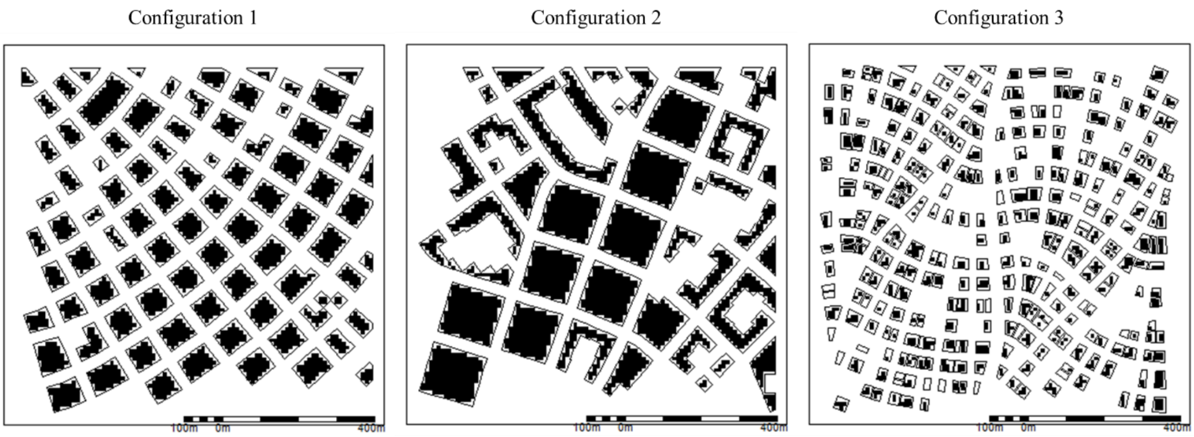

Figure 9: Definition of the three synthetic urban configurations (contour lines) and explicit representation of the buildings on a Cartesian grid of 10 m (dark areas).

4.2.1 *Description of the test cases*

The considered urban networks extend over a domain of 1 × 1 km^2 with a flat bottom and a uniform Manning roughness coefficient of $n = 0.04$ $sm^{-1/3}$.

A total inflow discharge of 200 m^3/s was prescribed uniformly along the left and bottom sides of the domain (upstream boundary). The following weir formula was used as downstream boundary condition along the right and top sides of the urban area:

$$q = 0.5\sqrt{2g\left(h-0.3\right)^3} \tag{13}$$

The average areas of the buildings of configurations 1, 2 and 3 are respectively 3,861 m^2, 8,423 m^2 and 744 m^2.

4.2.2 *Numerical models*

Different computations were performed for the three configurations:

- Reference values for the hydraulic variables were generated at a micro-scale of 1 m with the CS model (CS-1m.). The computed water depths and unit discharges are displayed in Figure S1 of the Supplemental data.
- Configurations 1 and 2 were computed at a coarse scale of 10 m. At this scale, the cell area remains more than one order of magnitude smaller than the average area of the buildings (Figure 9a,b), corresponding thus to meso-scale modelling. Computations were performed with the CS (CS-10m) and PS-A-1 models with merging ($\phi_{\min}$ = 0.5) considering different values for the drag coefficient c_D^0.
- Configuration 3 was simulated at the coarse scale of 10 m with the porosity models with merging ($\phi_{\min}$ = 0.1). The threshold $\phi_{\min}$ was taken at a lower value than for configurations 1 and 2 to reproduce more accurately the narrow streets between buildings. While some obstacles are physically represented in the computational domain (meso-scale), 10.6% of obstacles are only reproduced through the porosity parameters (macro-scale). The ability of PS-A-1 and PS-A-2 models to reproduce the reference results at the coarse scale is analysed and compared without drag term and with an optimal drag coefficient of $c_D^0 = 2$.

The water depths computed with the different numerical models are compared along the upstream boundary, while the distribution of the unit discharges is compared along the downstream boundary.

4.2.3 *Results*

Using the CS model at the coarse scale (CS-10m) for configurations 1 and 2, the water depth profiles along the upstream border are overestimated (Figure 10) and the coarse model errors on water depths $L_{3,h}$ are around 5% of the mean water depths (Figure 11). The PS-A-1 model without drag term underestimates the water depths; but the corresponding $L_{3,h}$ values decrease to around 2%. A very satisfactory reproduction of the water depth profiles is obtained with the drag term, for which the coarse model errors are reduced to about 0.5%.

The normal unit discharge profiles along the downstream borders are visually close to each other (Figures S2). Differences mainly occur at the extremities of the profiles where the flow does not cross the urban area. The coarse model errors on discharges $L_{3,q}$ are reduced by using the PS-A-1 models instead of the CS-10m model but are not significantly influenced by the drag term.

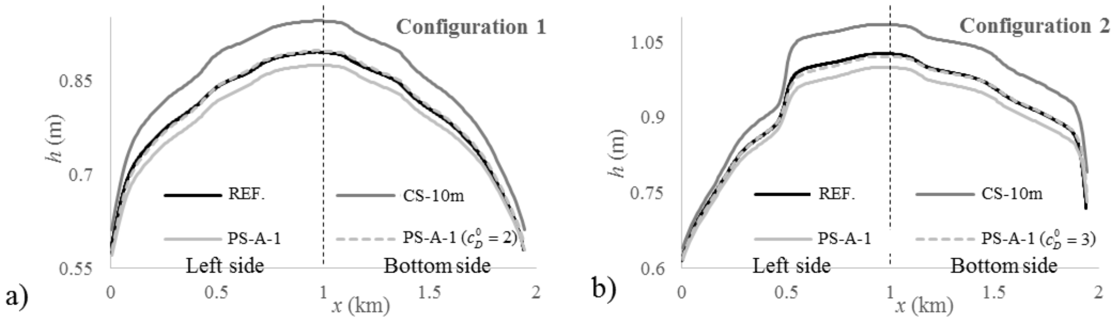

Figure 10: Computed water depths along the inflow boundaries, i.e. along the left and bottom sides of the urban area in configurations 1 (a) and 2 (b).

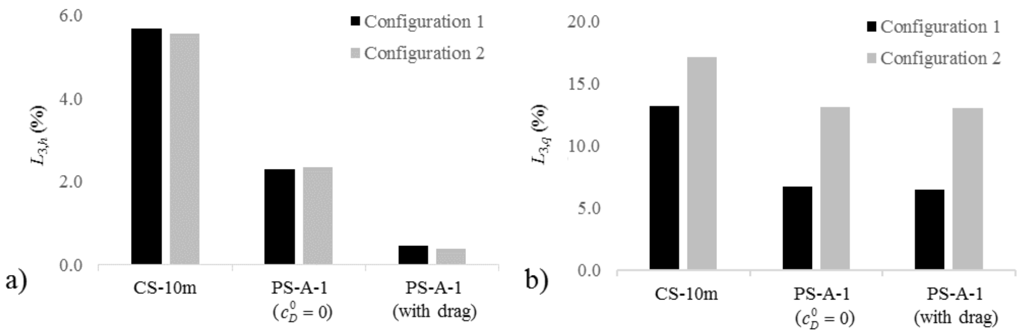

Figure 11: Coarse model errors L_3 on the water depth (a) and unit discharge profiles (b) for configurations 1 and 2.

In configuration 3, the water depths along the upstream boundary are underestimated with the PS-A-1 model and slightly overestimated with the PS-A-2 model when no drag term is considered (Figure 12). The results in Figure 13 show that, without any calibration ($c_D^0 = 0$), the PS-A-2 model ($L_{3,h} \approx 1\%$) performs significantly better than the PS-A-1 model ($L_{3,h} \approx 4\%$), for a configuration at the transition between meso- and macro- scale modelling. The PS-A-1 model with a drag term gives a value of the porosity model error on the water depth $L_{3,h}$ (0.5%) similar to the best values obtained for configurations 1 and 2. The normal unit discharges remain weakly affected by the method used for the determination of the conveyance porosities and by the drag term (Figures 13b and S3).

Overall, the three meso-scale configurations considered here reveal that evaluating the conveyance porosity parameters directly along the edges by the standard footprint method (i.e. model PS-A-1) leads to accurate results. Using the PS-A-1 model at a coarse scale of 10 m lead here to a reduction of the computational time by about two orders of magnitude compared to a simulation at a micro-scale of 1 m while preserving accuracies on the upstream water depths around 0.5% of the mean value.

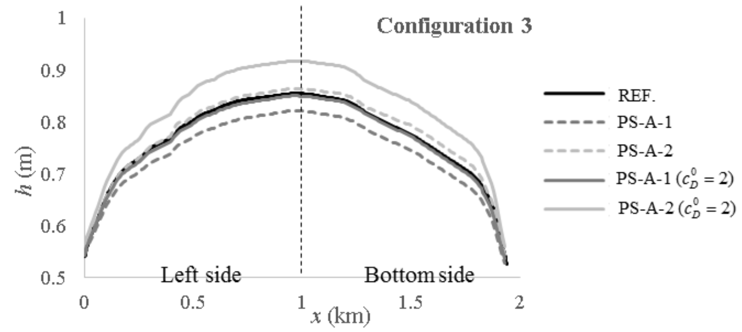

Figure 12: Computed water depths along the inflow boundaries, i.e. along the left and bottom sides of the urban area in configurations 3.

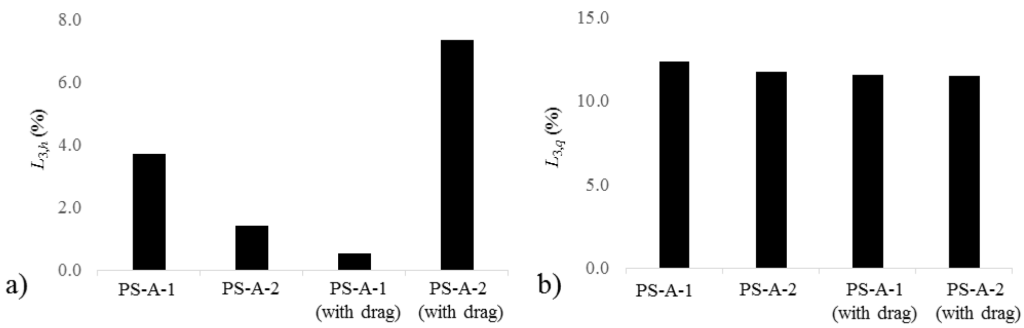

Figure 13: Porosity model errors L_3 on the water depth (a) and unit discharge profiles (b) for configuration 3 with a grid size of 10 m.

4.2.4 *Limitation of the scalar formulation of the drag term*

Additional computations were performed for Configuration 1 (Figure 9) with two different sets of flow boundary conditions (Table 4). The results presented in section 4.2.3 were obtained by considering inflow boundary conditions along the left and bottom sides of the urban area, and downstream boundary conditions along the right and top sides. Here, the computations were repeated by setting the inflow and outflow boundary conditions along two opposite sides of the domain (i.e. left and right, or bottom and top sides), while the two remaining sides were considered as impervious.

The profiles of computed water depths along the upstream sides of the urban area are displayed in Figure 14, which is similar to Figure 10. Compared to the results of a standard shallow-water model (CS-10m model), the water depths computed with the anisotropic porosity model (PS-A-1 model) are closer to the reference (CS-P predictions). For both the left-to-right and the bottom-to-top flow configurations, the coarse model errors on water depths $L_{3,h}$ range between 2% and 5% of the mean water depth when the drag coefficient is varied between $c_D^0 = 0.0$ and $c_D^0 = 2.0$. This is substantially lower than when no porosity model is used (10% with the CS-10m model).

The optimal values of the drag coefficient for the left-to-right and bottom-to-top flow configurations is the same ($c_D^0 = 0.5$). This is in agreement with the overall orientation of the network of streets almost along the diagonals of the computational domain, which makes the two flow configurations approximately equivalent. In contrast, we find that the optimal drag coefficient differs between the initial set of flow boundary conditions (section 4.2.3) and the two flow configurations considered here (left-to-right and bottom-to-top). In the former case, the optimal value of c_D^0 was equal to 2.0, whereas here the coarse model error on water depths is minimal when c_D^0 is reduced to 0.5. This result confirms a fundamental limitation of the scalar formulation of the drag term, which fails to capture the dependence of drag effects on the orientation of the main flow direction compared to the network of street. The loss in accuracy resulting form this limitation remains nonetheless lower than the enhancement in accuracy brought by the use of a porosity model instead of a standard shallow-water model (CS-10m). Although only tested so far for idealized periodic urban networks, the more advanced tensor formulation introduced by Velickovic et al. (2017) paves the way for the development of generalized drag models as needed for simulating complex urban flooding in realistic street networks.

Flow boundary conditions	According to section 4.2.1	Left-to-right	Bottom-to-top
Left side	Inflow boundary	Inflow boundary	Impervious
Right side	Outflow boundary	Outflow boundary	Impervious
Bottom side	Inflow boundary	Impervious	Inflow boundary
Up side	Outflow boundary	Impervious	Outflow boundary
Optimal drag coefficient	$c_D^0 = 2.0$	$c_D^0 = 0.5$	$c_D^0 = 0.5$

Table 4: Considered flow boundary conditions and corresponding optimal values of the drag coefficient.

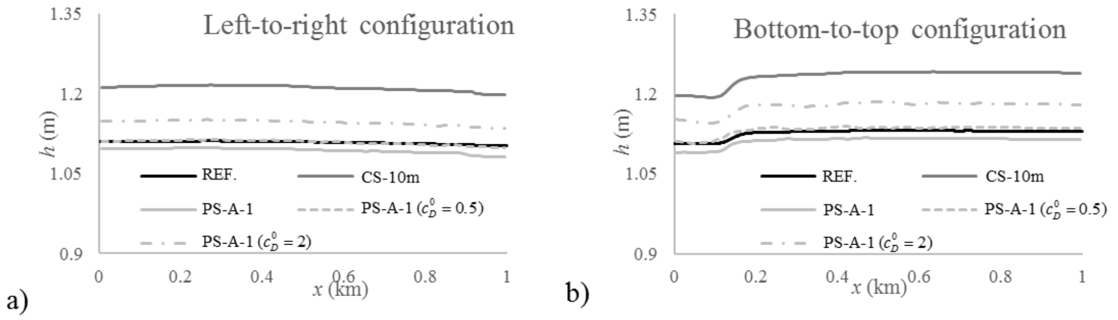

Figure 14: Water depths along the upstream boundaries in the “left-to-right” (a) and “bottom-to-top” (b) flow configurations.

4.3 *Dam-break flow over an anisotropic array of buildings*

4.3.1 *Test case description*

We consider a dam-break flow over an urban area consisting of 18 identical buildings of 20×20 cm^2, as shown in Figure 15 and described by Yoon (2007). The urban network is anisotropic as the street widths are different in both directions. Experimental measurements of the time evolution of water depths are available at 17 locations within and nearby the urban area. The initial water depth in the reservoir is 0.3 m. Transmissive boundary conditions are prescribed along the open sides of the floodplain. Consistently with Kim et al. (2015), we use the friction formula of Haaland (1983) with a Nikuradse sand-grain roughness height of $k_s = 3 \times 10^{-4}$ m.

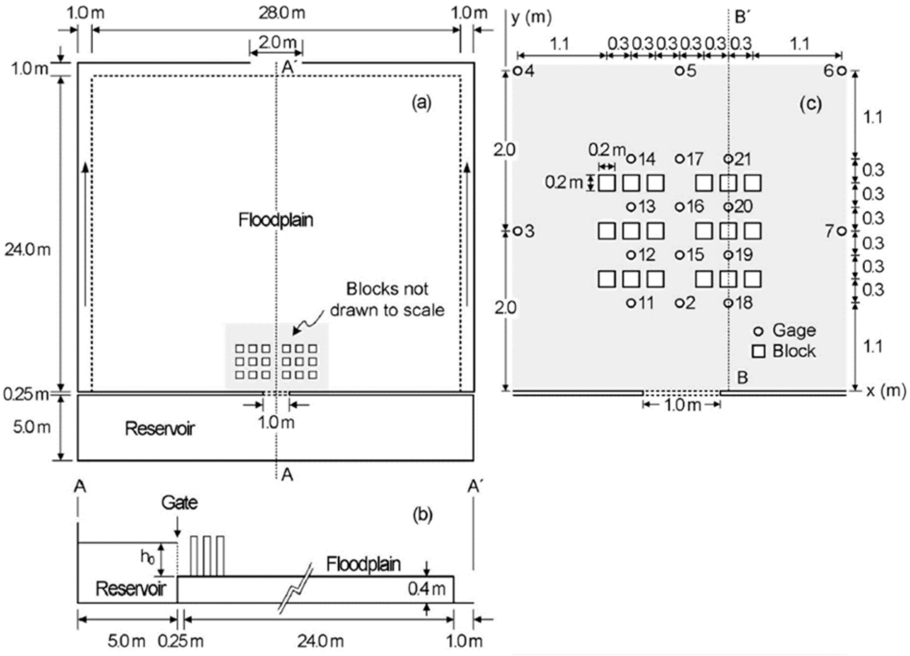

Figure 15: Experimental set-up of Yoon (2007), as described by Kim et al. (2015).

4.3.2 *Pore-scale error*

Reference results were generated by using the CS model with a fine resolution of 0.05 m. In this mesh, all computational cells are either filled by obstacles or entirely free for water. The micro-scale results of the CS model were then aggregated at the coarse scale of 0.25 m by averaging the flow variables of the cells not occupied by obstacles (CS-P predictions).

Comparing the CS-P predictions of water depths to the measurements, the pore-scale error L_{1+2} (averaged over all time steps and all stations) is around 0.68 cm, which represents 16% of the average measured water depths over the first 300 sec.

4.3.3 *Tested porosity models*

Kim et al. (2015) applied an unstructured porosity model to reproduce the experimental results with a gap-conforming mesh and cell sizes ranging between 0.25 m and 0.33 m. Here, we apply porosity models on a Cartesian grid with a resolution of 0.25 m.

Since the cell size is larger than the building size, the discretisation corresponds to macro-scale modelling. We compare the results obtained with the PS-A-1 and PS-A-2 models. Because the optimal drag coefficient c_D^0 is known to depend on the model used (Kim et al., 2015; Özgen et al., 2016), four values of c_D^0 (1, 2, 3 and 4) were tested in combination with each model.

Since the positive wave crosses the two blocks of buildings in a few seconds, which is negligible compared to the total transient phase of 600 seconds, the transient momentum dissipation model is not useful in this *quasi-steady* test case.

4.3.4 *Influence of porosity model and drag coefficient*

As shown in Table 5, the PS-A-2 model, which captures the presence of nearby obstacles, gives in all cases more accurate results than the PS-A-1 model, in which the conveyance porosity is evaluated locally at the edges. This difference prevails both for the total error L_0 and for the porosity model error L_3, evaluated either for water depth or for flow velocity.

The drag coefficient minimizing the porosity model errors L_3 corresponds to $c_D^0 = 3$ when considering the water depths and $c_D^0 = 2$ for the fluid velocities; but both values perform actually very similarly. Based on an unstructured mesh, Kim et al. (2015) reported an optimal value of $c_D^0 = 1$ for both hydraulic variables, which suggests some dependence of the optimal drag coefficient on the porosity model used.

The minimum value for porosity model errors on water depths with the Cartesian grid ($L_{3,h}$ = 0.32 cm) is twice lower than the pore-scale error.

	PS-A-1				PS-A-2			
	$c_D^0=1$	$c_D^0=2$	$c_D^0=3$	$c_D^0=4$	$c_D^0=1$	$c_D^0=2$	$c_D^0=3$	$c_D^0=4$
$L_{0,h}$	1.58 (36%)	1.44 (33%)	1.04 (24%)	0.87 (20%)	1.07 (24%)	0.92 (21%)	0.85 (19%)	0.81 (18%)
$L_{3,h}$	1.13 (28%)	0.97 (24%)	**0.51 (13%)**	0.60 (15%)	0.53 (13%)	0.36 (9%)	**0.32 (8%)**	0.33 (8%)
$L_{3,V}$	18.6 (28%)	22.3 (34%)	**16.6 (25%)**	21.6 (33%)	15.0 (23%)	**14.0 (21%)**	15.3 (23%)	16.9 (26%)

Table 5: Total errors L_0 and porosity model errors L_3 for water depths (cm) and velocity magnitudes (cm/s). The relative values in brackets are determined by comparing the absolute values to the average of the reference flow variables over the firsts 300 sec.

4.3.5 *Time series*

Figure 16 compares the time evolution of water depths predicted by the PS-A2 model ($c_D^0=3$) to the reference computation (CS-P) and to the observations at different gage stations. The results show that the differences between the observations and the CS-P predictions are distinctively higher than those between the PS-A-2 model and the CS-P values. Additionally, the PS-A-2 model captures satisfactorily the peak values and the time evolution of the water depths at most stations. As shown in Figure S4, the CS-P predictions for velocity magnitudes are fairly well reproduced by the PS-A-2 model for most stations except along the centreline, were high velocities occur. This was also noticed by Kim et al. (2015).

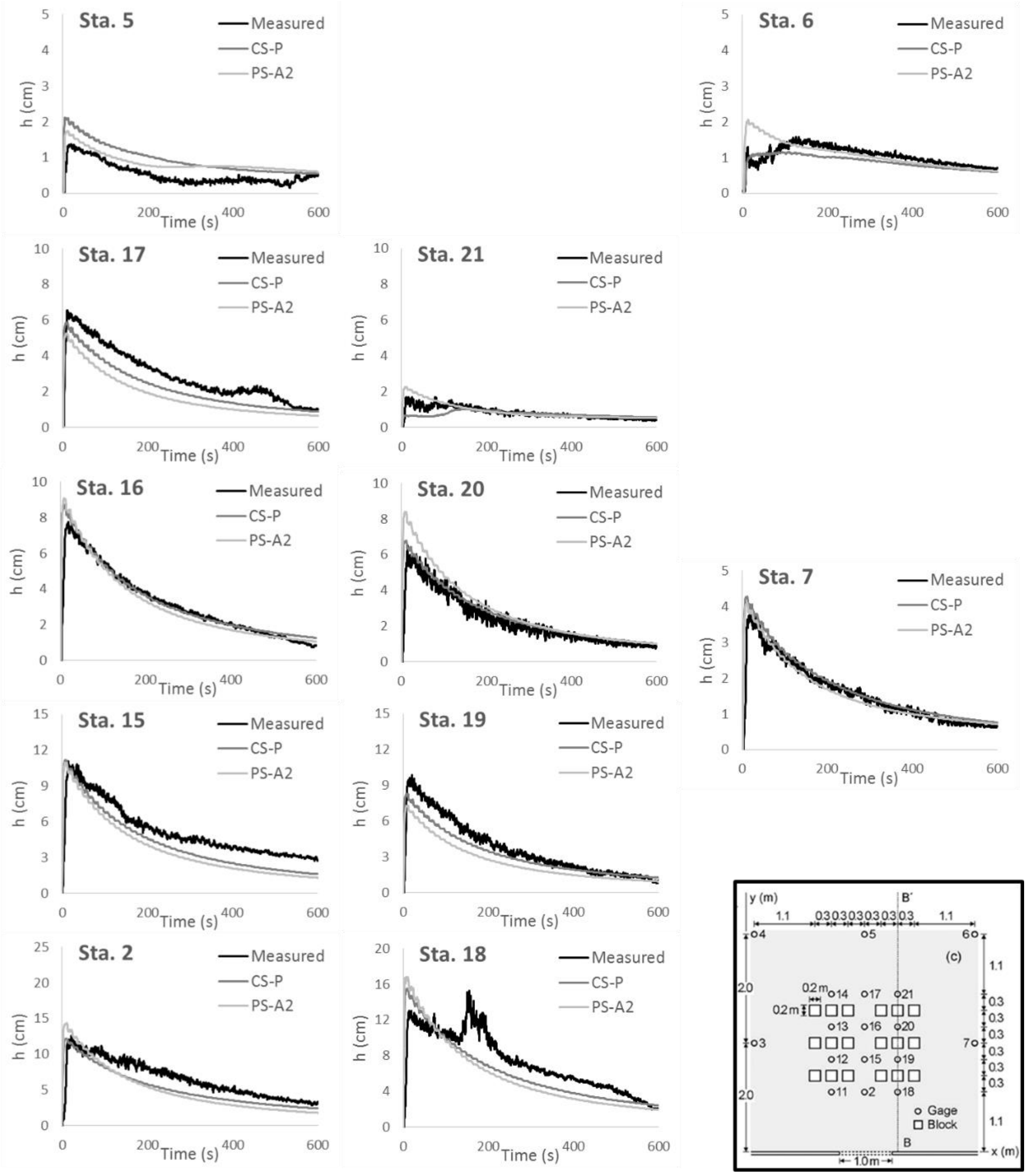

Figure 16: Comparison of water depth measurements, CS-P predictions and computations with the PS-A-2 model using the optimal value of $c_D^0 = 3$ for water depths.

4.4 *Idealized urban network*

The potential benefit of discriminating the porosity parameters between the different terms of the governing equations (PS-A-D model in Table 1) is discussed here for an idealized urban network made of single-size aligned buildings. Key flow features can be estimated a priori because of the simple geometry of the urban network. Therefore, the values of the porosity parameters may be set to reproduce the expected impact of obstacles on each term. The results computed with the PS-A-D model are also compared to those of the PS-I, PS-A-1 and PS-A-1-D models.

4.4.1 *Description of the test case*

The considered domain is divided into four parts (Part I to Part IV from upstream to downstream in Figure 17), all with a frictionless bottom. Parts I to III are flat while a slope of 10% is introduced in Part IV to prescribe a transmissive boundary condition at the downstream end. Part II is made of a symmetric and isotropic urban network in which the building grid is aligned with the main flow direction. The average storage porosity in part II is equal to 0.75. A uniform unit discharge of 10 m^2/s is prescribed at the upstream end over the entire width.

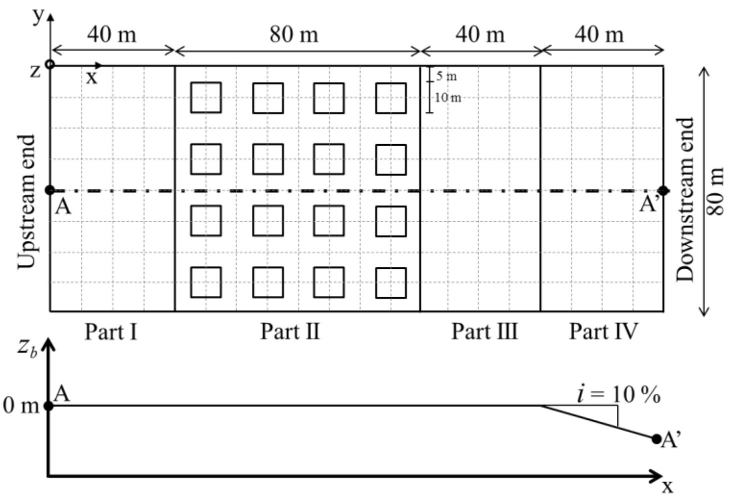

Figure 17: Idealized urban network: simulation domain and discretization at the coarse scale.

4.4.2 *A priori estimation of porosity parameters for the PS-A-D model*

We first estimate the porosity parameters to be used in the governing equations of the PS-A-D model so that this model mimics the micro-scale model. Based on a simplified, yet realistic, description of the flow field (Figure S5 in Supplemental data), we assume *(i)* a uniform value h_e of water depth in the urban network; *(ii)* no transverse velocity and a uniform streamwise velocity u_e in the streets aligned with the x-axis; *(iii)* negligible velocities in the wake of buildings.

Consequently, the macro scale water depths $\langle h \rangle$ and velocities $\langle u \rangle$ and $\langle v \rangle$ within a coarse cell of the urban area are estimated by:

$$\begin{cases} \langle h \rangle = h_e \\ \langle u \rangle = \dfrac{1/2\Delta x \Delta y}{3/4\Delta x \Delta y} u_e = \dfrac{2}{3} u_e \\ \langle v \rangle = 0 \end{cases}, \tag{14}$$

with Δx and Δy the lengths of the cell edges.

Based on this a priori estimation of the flow field and considering that the streamwise velocity component occurs over one-half of the length of the edges normal to the streamwise direction, the fluxes at these edges may be estimated by:

$$[\mathbf{F}]\,\partial\Omega = \begin{bmatrix} h_e u_e & 0 \\ \left(h_e u_e^2 + 0\right) & 0 \\ 0 & 0 \end{bmatrix} \frac{\Delta x}{2} \tag{15}$$

Using Eq. (14) to express the a priori estimation of the flow variables h_e and u_e as a function of the coarse scale variables leads to:

$$[\mathbf{F}]\,\partial\Omega = \begin{bmatrix} \frac{3}{2}\langle h \rangle \langle u \rangle & 0 \\ \frac{9}{4}\langle h \rangle \langle u \rangle^2 & 0 \\ 0 & 0 \end{bmatrix} \frac{\Delta x}{2} \tag{16}$$

Assuming a constant reconstruction of the flow variables from the cells to the edges and comparing Eq. (16) to Eq. (9), this leads to the following estimation of the porosity parameters: $\psi_c = 3/4$ and $\psi_{m,A_1} = 9/8$. These values are consistent with the condition $\psi_{mA_1} \geq \psi_c$ ensuring the hyperbolicity of the system of equations. The edge porosity parameter ψ_{m,A_1} used for the computation of the advective term is higher than 1. This results from the macro scale value $\langle u \rangle^2$ being lower than half of u_e^2: $\langle u \rangle^2 = 4/9 u_e^2$.

Since the pressure fluxes vanish in the case of a horizontal free surface, the corresponding edge porosity $\psi_{m,P}$ remains undetermined. Therefore, we have analysed the sensitivity of the results to the value of $\psi_{m,P}$ by testing $\psi_{m,P} = 0.5$ and $\psi_{m,P} = 1.0$ (PS-A-D0.5 and PS-A-D1.0 models, respectively).

Note that, at the edges partly occupied by an obstacle, the porosity parameters are identical in the PS-A-D0.5 and PS-A-1-D models ($\phi = 3/4$ and $\psi = 1/2$). In contrast, along the edges free of obstacles, the value of ϕ remains the same (ϕ = 3 / 4) but the values of ψ are different: ψ = 1 / 2 in the PS-A-D0.5 model and ψ = 1 in the PS-A-1-D model.

4.4.3 *Results and discussion*

Here, micro-scale modelling refers to a cell size of 1 m and the coarse scale models are based on a cell size of 10 m. We consider as a reference the results computed with the CS model at the micro-scale (CS-1m), averaged over the coarse cells of 10 m (CS-P predictions). Hence, these reference data incorporate the scale error. Hydraulic variables computed with the different models are compared along the longitudinal profile A-A’ (Figure 17). As shown in Figure 18, the results reveal the following.

- In the urban area (Part II), the free surface levels and velocities computed with the micro-scale CS-1m model do not evolve significantly. The unit discharge in this part (~22 m^2/s) is slightly higher than twice the uniform discharge prescribed at the upstream end (10 m^2/s). This tends to confirm that the flow is concentrated along the longitudinal streets free of obstacles, as assumed in the a priori estimation of the flow field.
- The scale error between the CS-1m model and CS-P values are generally limited for the water depths; but they are significant for the dynamic variables. At the downstream end, differences between CS-1m and CS-P are related to the cross-waves expanding from downstream of the building area. The scale errors between CS-1m and CS-P are generally lower than the porosity model errors for water depths while they are higher for velocities and unit discharges. This shows a strong dependence of the scale error on the considered flow variable.

- The PS-I, PS-A-1 and PS-A-1-D models underestimate the water depths and overestimate the velocities in the urban area when no drag term is used. Using the PS-A-1 model, an optimal value of the drag coefficient regarding the reproduction of the free surface level at the upstream end was found equal to $c_D^0 = 1.75$. In the urban area (Part II), the PS-A-1 model with an optimal drag coefficient overestimates the water depths. PS-I, and PS-A-D (same results for $c_D^0 = 0$ and $c_D^0 = 1.75$) models enable a good reproduction of unit discharges in the urban area while the PS-A-1 and PS-A-1-D (same results for PS-A-D1.0 and PS-A-D0.5 models) model induces oscillations. These oscillations result from the changes in the value of the porosity parameters from one edge to the following one. The PS-A-D0.5 model reproduces all flow variables with a good accuracy.

These results show that discriminating the porosity parameters between the various terms of the governing equations based on considerations of the flow dynamic can improve the reproduction of the effects of the obstacles on these terms. However, such a discrimination is feasible in practice only for simple urban networks for which general characteristics of the flow pattern can be estimated a priori. It remains hardly transferable to more complex urban geometries due to the lack of an ad hoc methodology.

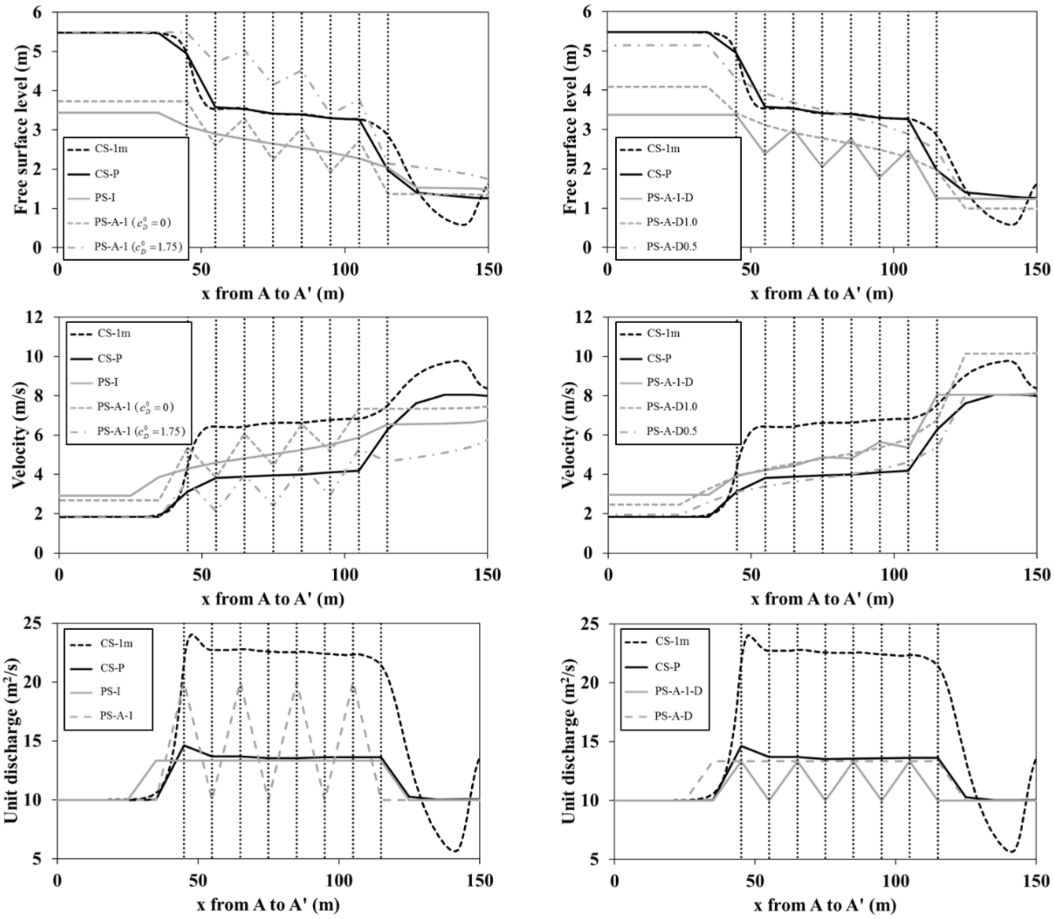

Figure 18: Free surface levels, velocity magnitudes and unit discharges along A-A’ for the different models. Vertical dotted lines represent the location of the buildings.

4.5 *Wave propagation*

We consider a dam-break flow over a horizontal and frictionless bottom with a large number of obstacles as represented in Figure 19. This test case is similar to those introduced by Guinot (2012) and used by Özgen et al. (2016) and Guinot et al. (2017). The initial water depth is 10 m for negative abscissa and 1 m for positive ones.

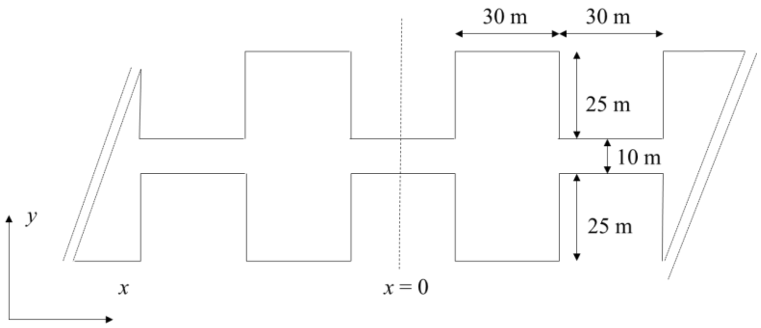

Figure 19: Channel geometry for the test case assessing wave propagation.

Computations were performed with a fine resolution CS model (1 m) and with the porosity models PS-A-D1.0 ($\psi_{mP} = 1.0$) and PS-A-D1/6 ($\psi_{mP} = 1/6$, consistently with the geometry of the contraction) using a cell size of 60 m. The transient momentum dissipation coefficient μ was calibrated to reproduce optimally the propagation speed of the front of the positive wave. Using a similar a priori estimation of the flow field as for the test case of section 4.4, the porosity parameters are $\phi = 7/12$, $\psi_c = 7/12$ and $\psi_{mA} = 49/24$. These values turn out to be identical to those derived with the dual integral porosity model (Guinot et al., 2017) if the cell edges are located at the contractions ($\phi_\Omega = 7/12$ and $\phi_\Gamma = 1/6$, leading to $\phi = 7/12$, $\psi_c = \phi = 7/12$, and $\psi_{mA} = \phi_\Gamma \beta^2 = \phi_\Omega^2 / \phi_\Gamma = 49/24$). This is a remarkable result, since the two estimations of the porosity parameters stem from two independent lines of reasoning.

The computed water depths profiles are shown in Figure 20 at the time t = 200 s. As reported by Guinot et al. (2017), the transient momentum dissipation model enables a considerable improvement in the reproduction of the speed of positive waves. Like in section 4.4, PS-A-D model provides more accurate results if the edge porosity ψ_{mP} is representative of the smallest free length (PS-A-D1/6 model). This supports the closure model introduced by Guinot et al. (2017). Surprisingly, the value of the optimal transient momentum dissipation coefficient (μ = 0.60) is quite different from the one ($\mu = 0.41$) obtained by Guinot et al. (2017), showing the high sensitivity of this coefficient to the geometry which is here slightly different from the geometry used by Guinot et al. (2017).

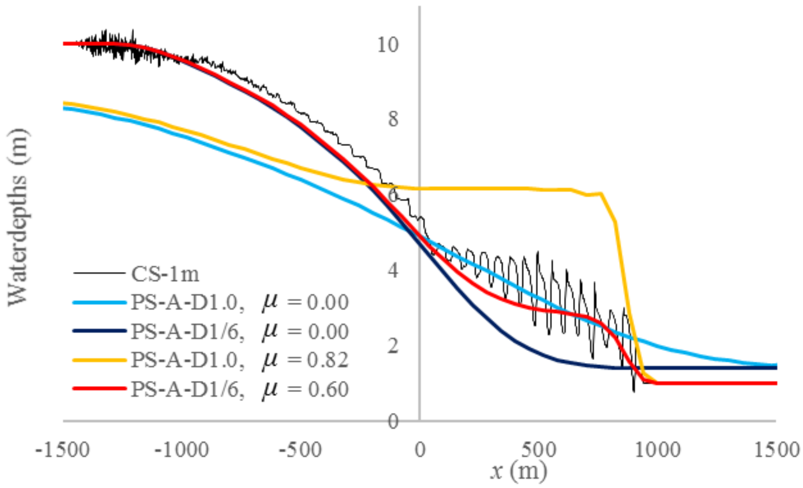

Figure 20: Comparison of the water depth profiles between the refined CS models and the PS-A-D models at t = 200 s.

5 CONCLUSION

The main contributions of this paper are three improvements of porosity-based models on Cartesian grids: *(i)* the use of a merging technique for cells with low storage porosity values, leading to a high increase in computational efficiency, *(ii)* the comparison of different methods for the determination of edge porosity parameters on Cartesian grids and *(iii)* a discussion of the potential benefit of distinguishing the values of flow-dependent porosity parameters to be used in the different terms of the governing equations.

- At the meso-scale, cells with low storage porosity values reduce significantly the computational efficiency due to the stability condition. We implemented a technique which consists in merging cells having a storage porosity below a threshold to neighbouring cells. In the case of a rectangular channel discretised on a Cartesian grid, this technique enables both accurate and efficient computations.
- We defined two different modelling scales depending on the relative sizes of obstacles compared to the cell size. At the "meso-scale", the obstacles remain explicitly discretized on the grid, while at the "macro-scale", the presence of obstacles is reflected only through the porosity parameters. In the case of porosity models applied on Cartesian grids, we found that

the optimal method for evaluating the conveyance porosity depends on the modelling scale. At the meso-scale, the obstacles intersect the computational edges and the conveyance porosity can therefore be evaluated directly along the edges. In contrast, at the macro-scale, the presence of obstacles not intersecting the cell edges must be considered when evaluating the conveyance porosities. Based on a dedicated test case involving synthetic urban networks, we found that taking the minimum fraction of free length parallel to the edge over half of a cell on either sides of the edge gives more accurate results than the determination of the conveyance porosity locally along the edges.

- In our derivation of the porosity model we introduced different porosity parameters in the different terms of the governing equations. Considering an idealized urban network for which key features of the flow field can be estimated a priori, we estimated physically relevant values for each porosity parameter, reflecting the specific effect of obstacles on each term of the governing equations at the coarse scale. While this approach proved promising, its generalization to more complex flows remains challenging.

The above-mentioned porosity models consider that the obstacles are sufficiently high so that they cannot be overtopped by the flood. The porosity parameters are therefore independent of the flow depth. Özgen et al. (2016) introduced recently a depth-dependent anisotropic porosity model to consider the possible submergence of low-level obstacles. This is certainly a path to follow for further generalizing the model presented here.

ACKNOWLEDGEMENTS

The research was funded through the ARC grant for Concerted Research Actions, financed by the Wallonia-Brussels Federation. The authors are grateful to Prof. B. Sanders and B. Kim for sharing experimental data for the dam-break flow over an anisotropic array of building.

REFERENCES

Arrault, A., Finaud-Guyot, P., Archambeau, P., Bruwier, M., Erpicum, S., Pirotton, M., Dewals, B., 2016. Hydrodynamics of long-duration urban floods: Experiments and numerical modelling. Natural Hazards and Earth System Sciences 16, 1413–1429.

Brazdova, M., Riha, J., 2014. A simple model for the estimation of the number of fatalities due to floods in central Europe. Natural Hazards and Earth System Sciences 14, 1663–1676.

Brodtkorb, A.R., Sætra, M.L., Altinakar, M., 2012. Efficient shallow water simulations on GPUs: Implementation, visualization, verification, and validation. Computers and Fluids 55, 1–12.

Bruwier, M., Archambeau, P., Erpicum, S., Pirotton, M., Dewals, B., 2016. Discretization of the divergence formulation of the bed slope term in the shallow-water equations and consequences in terms of energy balance. Applied Mathematical Modelling 40, 7532–7544.

Causon, D.M., Ingram, D.M., Mingham, C.G., Yang, G., Pearson, R.V., 2000. Calculation of shallow water flows using a Cartesian cut cell approach. Advances in Water Resources 23, 545–562.

Chen, A.S., Evans, B., Djordjević, S., Savić, D.A., 2012. A coarse-grid approach to representing building blockage effects in 2D urban flood modelling. Journal of Hydrology 426–427, 1–16.

Costabile, P., Macchione, F., 2015. Enhancing river model set-up for 2-D dynamic flood modelling. Environmental Modelling and Software 67, 89–107.

De Moel, H., Van Alphen, J., Aerts, J.C.J.H., 2009. Flood maps in Europe - Methods, availability and use. Natural Hazards and Earth System Science 9, 289–301.

Dottori, F., Di Baldassarre, G., Todini, E., 2013. Detailed data is welcome, but with a pinch of salt: Accuracy, precision, and uncertainty in flood inundation modeling. Water Resources Research 49, 6079–6085.

EEA, 2010. Mapping the impacts of natural hazards and technological accidents in Europe An overview of the last decade. Copenhagen: European Environment Agency (EEA).

El Kadi Abderrezzak, K., Paquier, A., Mignot, E., 2009. Modelling flash flood propagation in urban areas using a two-dimensional numerical model. Natural Hazards 50, 433–460.

Erpicum, S., Dewals, B.J., Archambeau, P., Pirotton, M., 2010. Dam-break flow computation based on an efficient flux-vector splitting. Journal of Computational and Applied Mathematics 234, 2143–2151.

Guinot, V., 2012. Multiple porosity shallow water models for macroscopic modelling of urban floods. Advances in Water Resources 37, 40–72.

Guinot, V., Sanders, B.F., Schubert, J.E., 2017. Dual integral porosity shallow water model for urban flood modelling. Advances in Water Resources 103, 16–31.

Guinot, V., Soares-Frazão, S., 2006. Flux and source term discretization in two-dimensional shallow water models with porosity on unstructured grids. International Journal for Numerical Methods in Fluids 50, 309–345.

Haaland, S.E., 1983. Simple and explicit formulas for the friction factor in turbulent flow. Journal of Fluids Engineering, Transactions of the ASME 105, 89–90.

Kellermann, P., Schöbel, A., Kundela, G., Thieken, A.H., 2015. Estimating flood damage to railway infrastructure - The case study of the March River flood in 2006 at the Austrian Northern Railway. Natural Hazards and Earth System Sciences 15, 2485–2496.

Kim, B., Sanders, B.F., Famiglietti, J.S., Guinot, V., 2015. Urban flood modeling with porous shallow-water equations: A case study of model errors in the presence of anisotropic porosity. Journal of Hydrology 523, 680–692.

Kim, B., Sanders, B.F., Schubert, J.E., Famiglietti, J.S., 2014. Mesh type tradeoffs in 2D hydrodynamic modeling of flooding with a Godunov-based flow solver. Advances in Water Resources 68, 42–61.

Kreibich, H., Van Den Bergh, J.C.J.M., Bouwer, L.M., Bubeck, P., Ciavola, P., Green, C., Hallegatte, S., Logar, I., Meyer, V., Schwarze, R., Thieken, A.H., 2014. Costing natural hazards. Nature Climate Change 4, 303–306.

Özgen, I., Zhao, J., Liang, D., Hinkelmann, R., 2016. Urban flood modeling using shallow water equations with depth-dependent anisotropic porosity. Journal of Hydrology 54, 1165-1184.

Sanders, B.F., Schubert, J.E., Gallegos, H.A., 2008. Integral formulation of shallow-water equations with anisotropic porosity for urban flood modeling. Journal of Hydrology 362, 19–38.

Schubert, J.E., Sanders, B.F., 2012. Building treatments for urban flood inundation models and implications for predictive skill and modeling efficiency. Advances in Water Resources 41, 49–64.

Valiani, A., Begnudelli, L., 2006. Divergence form for bed slope source term in shallow water equations. Journal of Hydraulic Engineering 132, 652–665.

Velickovic, M., Zech, Y., Soares-Frazão, S., 2017. Steady-flow experiments in urban areas and anisotropic porosity model. Journal of Hydraulic Research 55(1), 85-100, 2017.

Yoon, K., 2007. Experimental Study on Flood Inundation Considering Urban Characteristics (FFC06-05). Urban Flood Disaster Management Research Center, Seoul.

APPENDIX A. DERIVATION OF THE EIGENVALUES OF THE GOVERNING EQUATIONS

Considering an infinitesimal control volume, a horizontal and frictionless bottom and applying the divergence theorem for continuous and differentiable solutions, the governing equations are rewritten in a differentiable formulation for a one-directional flow (Guinot et al., 2017):

$$\partial_t\left(\phi\begin{bmatrix} h \\ uh \\ vh \end{bmatrix}\right)+\partial_x\left(\begin{bmatrix} \psi_c uh \\ (1-\mu)\left(\psi_{mA_1}u^2h+\psi_{mP}\dfrac{gh^2}{2}\right) \\ (1-\mu)\psi_{mA_2}uvh \end{bmatrix}\right)=0 \tag{17}$$

The corresponding Jacobian matrix **A** is:

$$\mathbf{A}=\frac{1}{\phi}\begin{bmatrix} 0 & \psi_c & 0 \\ (1-\mu)\left(\psi_{mP}c^2-\psi_{mA_1}u^2\right) & 2(1-\mu)\psi_{mA_1}u & 0 \\ -(1-\mu)\psi_{mA_2}uv & (1-\mu)\psi_{mA_2}v & (1-\mu)\psi_{mA_2}u \end{bmatrix} \tag{18}$$

with $c=\sqrt{gh}$.

The eigenvalues for the one-directional case are:

$$\begin{aligned} \lambda_1 &= (1-\mu)\frac{\psi_{mA_1}}{\phi}u-c' \\ \lambda_2 &= (1-\mu)\frac{\psi_{mA_2}}{\phi}u \\ \lambda_3 &= (1-\mu)\frac{\psi_{mA_1}}{\phi}u+c' \end{aligned} \tag{19}$$

with $c'=\sqrt{(1-\mu)\left(\dfrac{\psi_{mA_1}}{\phi^2}u^2\left[(1-\mu)\psi_{mA_1}-\psi_c\right]+\dfrac{\psi_c\psi_{mP}}{\phi^2}c^2\right)}$.

If the values of the edge porosity parameters are replaced by the corresponding values according to Table 1 for model PS-A-1-D (i.e. DIP model, with $\psi_{mA_1} = \psi_{mA_2} = \phi^2/\psi$; $\psi_c = \phi$, and $\psi_{mP} = \psi$,), the same eigenvalues as computed by Guinot et al. (2017) are retrieved.

To ensure the existence of the eigenvalues in Eq. (19), configurations leading to $\psi_c > (1-\mu)\psi_{mA_1}$ should be excluded. For steady and quasi-steady flows (μ being set to zero), the hyperbolicity of the system is hence ensured when $\psi_{mA_1} \geq \psi_c$.